

Nano-confined controllable crystallization in supramolecular polymeric membranes for ultra-selective desalination

Received: 19 September 2024

Accepted: 19 February 2025

Published online: 07 March 2025

 Check for updates

Gang Lu¹✉, Hubao A², Yuanyuan Zhao³, Yan Zhao⁴, Hengyue Xu⁵, Wentao Shang⁶, Xi Chen¹, Jiawei Sun¹, Huacheng Zhang⁷, Jun Wu⁸, Bing Dai⁹, Bart Van der Bruggen⁴, Raf Dewil^{4,10}, Alicia Kyoungjin An^{1,11}✉ & Shuang Zheng^{12,13}✉

Innovations in self-assembly and aggregate engineering have led to membranes that better balance water permeability with salt rejection, overcoming traditional trade-offs. Here we demonstrate a strategy that uses multivalent H-bond interactions at the nano-confined space to manipulate controllable and organized crystallization. Specifically, we design amphiphilic oligomers featuring hydrophobic segments with strongly polar end-capped motifs. When spreading on air/water interfaces, the hydrophobic parts repel water, yielding an ordered alignment of supramolecular oligomers under nano-confinement, while the strongly polar sections engage in strong hydrogen bonding and reconfigure to strongly interact with water molecules, enabling the controlled assembly and orientation of nano-confined crystalline domains. This arrangement provides dual benefits: refining the distribution of pore sizes for ultra-selectivity and boosting the free volume for water permeation. Compared to counterpart oligomers with weakly polar motifs, the optimized membrane with a 6-nm thickness demonstrates the water permeability of $14.8 \text{ L m}^{-2} \text{ h}^{-1} \text{ bar}^{-1}$ and extraordinary water/NaCl selectivity of more than 54 bar^{-1} under pressure-driven condition. This study sheds light on how nano-confined self-assembly and aggregate engineering affect the architectures, functionality, and performance of polymer membranes, emphasizing the promise of controllable crystallization in ultrathin membranes for optimal desalination.

Developing membrane materials with superior permeability-selectivity performance is critical to energy-efficient desalination and fit-for-purpose water treatment^{1–3}, and advancing membrane selectivities has been identified as a new frontier of separation sciences^{4,5}. Existing dense and nanoporous polymeric membranes have highly heterogeneous internal structures of free volumes and pores^{6,7}, frustrating the rational design of materials to achieve more precise distinguishment of solutes.

To address these challenges, engineering membrane free volumes or nanopores with narrow size distribution is a crucial approach to achieving precise solute selectivities while preserving permeability^{8,9}. One method to customize pore size involves controlling the kinetics of interfacial polymerization (IP)^{10–13}. For instance, self-assembled surfactant networks promote quicker and more uniform monomer diffusion across oil/water interfaces during IP reactions, resulting in polyamide membranes with more consistent sub-nanometre pores¹³. Another approach

A full list of affiliations appears at the end of the paper. ✉ e-mail: ganglu2-c@my.cityu.edu.hk; alicia.kjan@ust.hk; shuang.zheng@dpag.ox.ac.uk

incorporates large molecules, such as macrocycles with permanent cavities or artificial water channels, into polymer membranes^{14–16}. Selectively functionalized macrocycles, for example, tend to arrange in an ordered manner, aligning their internal cavities to create straight sub-nano percolation channels¹⁵. Additionally, nanoscale management of internal inhomogeneity has proven effective^{6,17}. A cellulose triacetate membrane treated with a plasticizer demonstrated a reduced crystallite size and decreased salt flux without affecting water flux, indicating an improved water/salt selectivity¹⁷. Molecular engineering has been widely adopted in the design and self-assembly of polymer materials^{18–22}, therefore, development of polymeric membranes with narrowed pore size distribution at the molecular level has great potentials for desalination yet has rarely been reported. Achieving high boron rejection and chlorine tolerance simultaneously in these membranes could provide a significant enhancement, complementing the existing capabilities of state-of-the-art reverse osmosis (RO) membranes.

In this work, we design amphiphilic oligomers (tetra-PCL-UPy) with star-shaped hydrophobic chains capped with polar 2-ureido-4-pyrimidinone (UPy) groups. This design allows for precise molecular arrangement at air/water interfaces, enabling nano-confined controllable crystallization (NCC) to achieve homogenous pore size distribution of ultrathin membranes. The controlled molecular assembly and orientation of tetra-PCL-UPy chains formed at nano-confined spaces effectively improve the fractional free volume and narrow the pore size distributions due to the hampered chain mobility and the rigid end-functioned UPy motifs. The NCC membrane with a 6-nm thickness displays remarkable mechanical robustness and durability, with a Young's modulus approaching 3 GPa. The resultant membrane advances the upper bound with a water permeability of $14.8 \text{ L m}^{-2} \text{ h}^{-1} \text{ bar}^{-1}$ and a water/NaCl selectivity of over 54 bar^{-1} in hydraulic pressure-

driven process with 1000 ppm NaCl solution and 10 bar pressure, showing its potential for ultra-selective desalination and extraordinary water permeability. The high water permeance is attributed to the morphological and structural factors such as hydrophilic and negatively charged surface, and improved fractional free volume, while the high water/NaCl selectivity results from the narrowed pore size distribution. Furthermore, high boron rejection, high chlorine resistance, and structural and desalination durability are achieved.

Results

Design and preparation of Tetra-PCL-UPy

In this study, we strategically designed and synthesized two tetra-oligomers, Tetra-PCL-OH and Tetra-PCL-UPy, featuring identical four-armed crosslinked PCL backbones (Fig. 1). Tetra-PCL-OH features hydroxyl terminal groups, while tetra-PCL-UPy is equipped with UPy end-capped units, to explore the importance of the end-group functionalization on the membrane performance. The star-shaped PCL backbones were chosen for their ability to facilitate controllable crystallization in nano-confined environment and to enhance mechanical properties due to their branched architecture. This geometry ensures that each arm aligns symmetrically, providing better spatial control over the crystallization process. The restricted environment provided by the sub-10 nm ultrathin membrane further promotes the alignment of these arms, enabling controllable crystallization. At the air/water interface, the hydrophobic PCL arms repel water, encouraging the alignment of the oligomers parallel to the interface, while the polar UPy groups engage in strong multivalent hydrogen bonding with water molecules. This interplay ensures that the oligomers are evenly distributed and consistently oriented during the crystallization process, enhancing structural precision.

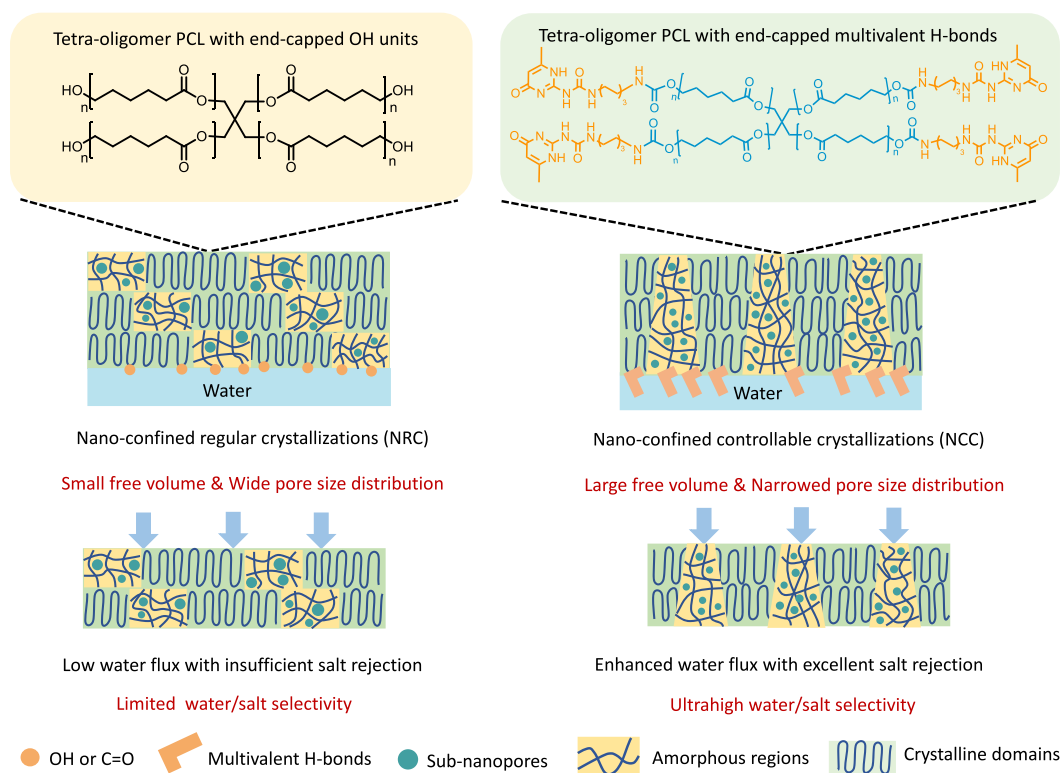


Fig. 1 | Schematic illustration of nano-confined crystallizations in polymer membranes for water-solute selectivity. Multivalent H-bond interactions can manipulate controllable and organized crystallization at the air/water interface under nanoconfinement. This arrangement offers dual benefits: refining the distribution of pore sizes for ultra-selectivity and boosting the free volume for

enhanced water permeation. Compared to nano-confined regular crystallization (NRC) membranes, nano-confined controllable crystallization (NCC) membranes exhibit a greater fractional free volume and a more refined pore size distribution, thus promoting water-salt selectivity.

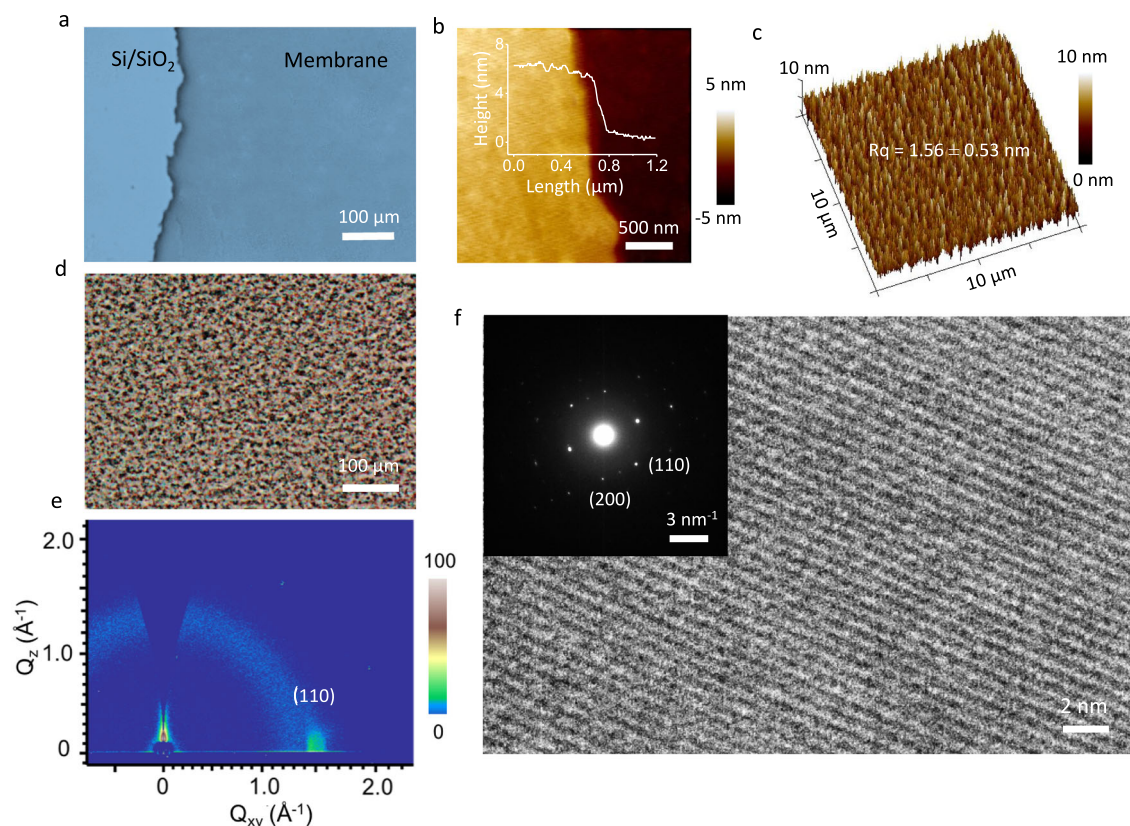


Fig. 2 | Characterizations of the NCC membrane. **a** An optical microscopy image of the NCC membrane located on a 300 nm SiO₂/Si wafer. **b** The membrane thickness profile of 6.2 ± 0.5 nm determined by AFM. **c** The roughness of the NCC membrane with 1.56 ± 0.53 nm. **d** The POM image of the NCC membrane showing

the birefringence pattern. **e** Two-dimensional GI-WAXS patterns of the nanofilm that was transferred on a silicon wafer. The most prominent Bragg reflection (110) was found. **f** HRTEM image and SAED pattern (inset) of the nanofilm. Error bars represent the standard deviation from three duplicate experiments.

To confirm the resulting tetra-oligomers, the ¹H NMR (Supplementary Figs. S1–3) and Fourier transform infrared (FTIR) spectroscopy (Supplementary Fig. S4) were performed. The three distinct amide proton peaks in the higher chemical shift region (between 9.0 and 14.0 ppm) were easily distinguishable from the aromatic and aliphatic protons, as shown in Supplementary Fig. S1, which is ascribed to the high spinning frequency. The three characteristic amide proton peaks were slightly shifted towards the downfield region (between 9.0 and 14.0 ppm) (Supplementary Fig. S3), indicating the occurrence of UPy dimerization and supramolecular polymerization via quadruple hydrogen bonding interactions²³. The FTIR spectrum revealed the disappearance of the isocyanate peak at approximately 2265 cm⁻¹ and the presence of the amide N-H unit in the final product of Tetra-PCL-UPy. The gel permeation chromatography (GPC) profiles (Supplementary Fig. S5) revealed an average molecular weight of around 10000 for both Tetra-PCL-OH and Tetra-PCL-UPy, while the polydispersity index (PDI) was measured to be 1.43 for Tetra-PCL-OH and 1.35 for Tetra-PCL-UPy.

Preparation of crystalline polymeric membranes

By leveraging the confined supramolecular assembly at the air/water interface, we have successfully fabricated ultrathin membranes with precise and organized crystalline structures. The fabrication process involves gently dropping a microdroplet of a polymer solution containing tetra-PCL-UPy dissolved in chloroform onto the water surface. As the solution rapidly spreads and evaporates at the air/water interface, a large-area membrane with controllable crystallization is formed under nano-confinement within seconds. This formation is facilitated by the synergistic effects of strong hydrogen bonding at the interface and hydrophobic interactions in the bulk phase. The hydrophobic PCL chains tend to pack closely together, whereas the polar UPy groups have a strong affinity for the water surface. The presence of strong

hydrogen bonding interactions at the air/water interface greatly hampers the mobility of tetra-PCL-UPy chains and creates an entropy barrier at the rear side, thus yielding a nano-confined controllable crystallization (NCC). Similarly, using the same process, microdroplets carrying tetra-PCL-OH can form nanofilms with nano-confined regular crystallization (NRC). In contrast to hydroxyl units, the quadruple hydrogen bonding of UPy motifs enhances the interfacial bonding with water molecules, leading to controllable crystallization in the NCC membranes. The membranes formed at the water/air interface can be easily transferred to various supports, such as polyethersulfone (PES) for desalination experiments, silicon wafers for measuring membrane thickness, and AAO for visual observation of the ultrathin membrane thickness. The nanofilm adheres firmly to the substrate surface due to the high density of interfacial non-covalent interactions. In addition, the resultant membranes can be labeled based on their thickness. For instance, the NCC-6 membrane has a ~6-nm thickness.

Characterizations of polymer nano-films

The NCC-6 membrane exhibited uniformity with clearly visible edges, as demonstrated by the optical microscope image (Fig. 2a and Supplementary Fig. S6). As displayed in Fig. 2b and Supplementary Fig. S7, the height profiles of the NCC-6 and NRC-6 membranes were 6.2 ± 0.5 nm and 6.4 ± 0.3 nm, respectively, as determined by atomic force microscopy (AFM). The NCC-6 membrane displayed a low root mean square roughness (Rq) of 1.56 nm for an area of $10 \times 10 \mu\text{m}$ (Fig. 2c), indicating a smooth surface. We also investigated the effect of the concentrations of the microdroplets on the membrane thickness and spreading area (Supplementary Figs. S8, 9). As the concentration ranged from 2 mg/mL to 40 mg/mL, the thickness of NCC nanofilms increased from ~6 nm to ~100 nm, and the spreading area would first increase and reach approximately 140 cm² at a concentration of

8 mg/mL and then reduced. The observed variation can be attributed to the changes in the spreading coefficient (S) (Supplementary Fig. S10 and Supplementary Table S1)^{24,25}. The spreading coefficient (S) is influenced by the balance of interfacial tensions between the polymer solution and the water phase. At low solute concentrations, the presence of tetra-PCL-UPy oligomers at the air/water interface lowers the interfacial tension, leading to an increase in S . This promotes the spreading of the nanofilm. As the solute concentration approaches 8 mg mL⁻¹, the oligomer molecules saturate the interface, maximizing the reduction in interfacial tension and achieving the largest spreading area. Beyond this concentration, further increases in solute concentration lead to the formation of a thicker polymer solution at the interface. This increases the viscosity of the solution, reducing its ability to spread freely. Additionally, excessive solute may lead to aggregation or hinder molecular mobility, thereby limiting the spreading area. As the spreading parameter (S) decreases, the spreading rate slows, potentially providing more time for PCL chains to interact and align. This may facilitate the folding and orientation of the chains, enhancing inter-chain interactions and contributing to an increase in membrane thickness. We then confirmed the crystalline nature of the NCC and NRC membranes through polarized optical microscopy (POM), differential scanning calorimetry (DSC), grazing incidence X-ray diffraction (GIXRD), and transmission electron microscopy (TEM). We adopted the polarization contrast enhancement technique to improve the phase contrast and interference effects^{26,27}, thus the POM image of the NCC-6 membrane showed bright birefringence patterns that originated from the strong chain alignment or crystals (Fig. 2d). In addition, NCC-6 showed a melting temperature of approximately 44 °C according to the second heating curve determined by DSC (Supplementary Fig. S11). As shown in the GIXRD images (Supplementary Fig. S12), the NCC membranes with different thicknesses exhibited three characteristic diffraction peaks, corresponding to the (110), (111), and (200) planes of the crystalline PCL polymer in the bulk phase. The NRC-6 membrane exhibited a crystallinity of approximately 32%, surpassing that of the NCC-6 membrane, which stands at 28.5% (Supplementary Fig. S13). Besides, the crystallinity of the NCC membranes slightly increased as the concentrations increased (Supplementary Fig. S14), due to the improved packing and orientation of PCL chains in the thicker membranes. We also made a plot of the spreading area and crystallinity of the NCC membranes (Supplementary Fig. S15). There was no uniform relationship as the crystallinity increased. To elucidate the alignment and orientations of the polymer chains, a Grazing-Incidence Wide-Angle X-ray Scattering (GI-WAXS) pattern was recorded (Fig. 2e). A significant Bragg reflection (110) was associated with q value of 1.51 Å⁻¹, which verified the crystalline nature and edge-on orientations of the tetra-PCL-UPy chains within the NCC-6 membrane. The TEM image (Fig. 2f) revealed that the morphology of the NCC membrane was highly oriented, and the distance between the lattice fringes was approximately 0.4 nm. The corresponding selected area electron diffraction (SAED) pattern confirmed high electron scattering and polymer single crystals of the NCC-6 membrane. Molecular and aggregate engineering can tailor the microscopic structures and pore sizes of membranes^{14–17}. We also measured the molecular weight cut-off (MWCO) of the NCC-6 and NRC-6 membranes using the rejection curves of neutral PEG molecules with molecular weights ranging from 200 to 800 Da (Supplementary Fig. S16). The MWCO of NCC-6 and NRC-6 were 237 Da and 375 Da, corresponding to pore radius of 0.28 nm and 0.36 nm, respectively. Moreover, compared with the NRC-6 membrane, the NCC-6 membrane exhibited a narrower pore size.

Controllable crystallization and Janus surface morphology

The controllable crystallization and Janus surfaces of the NCC-6 membrane were studied. The unconventional crystallization of NCC-6 on the top (facing the air phase) and rear (facing the water phase) surfaces was

studied by scanning electronic microscopy (SEM), Raman spectroscopy, and AFM. As indicated in the SEM images, the two sides of the NCC membrane on the silicon wafer were defect-free without showing any distinct differences (Supplementary Fig. S17). Raman spectra showed the crystalline peaks of the C-COO stretching band (911 cm⁻¹), C-C stretching band (1108 cm⁻¹), bending band (1441 cm⁻¹) and C=O stretching band (1723 cm⁻¹) on two sides of NCC-6 (Fig. 3a). The intensities of the C-C stretching band of the top side are more prominent than those of the rear side, as indicated by Raman mapping (Fig. 3b), suggesting the controllable crystallization of the two sides of the NCC-6 membrane. AFM based surface indentations (Fig. 3c–f) displayed the modulus profiles and distributions of the two sides of NCC-6 nanofilm. The upper surface displayed a greater abundance of crystals and a significantly higher Young's modulus (approximately 3 GPa) compared to the rear side, aligning with the controlled and organized crystallization observed in the NCC membrane. Conversely, both faces of the NRC-6 membrane exhibited a similar distribution of aggregated regions, as evidenced by the AFM phase images (Supplementary Fig. S18).

We subsequently confirmed the Janus morphology of the two sides of the NCC-6 membrane by water contact angle (WCA) measurement, zeta potential analysis and X-ray photoelectron spectroscopy (XPS). The WCAs of the top and rear side of NCC-6 are 59° ± 2° and 25° ± 1°, respectively (Fig. 3g). This Janus wetting property suggested that the two sides of the NCC-6 membrane had different chemical compositions and hydrophilic functionalities. The hydrophilic surface of NCC-6 contributes to rapid water diffusion and transport. However, for NRC-6 membrane, WCA of the top side is slightly higher than that of the rear side, indicating less pronounced Janus wetting properties (Supplementary Fig. S19).

We proposed a mechanism for the controllable crystallization and Janus surface of NCC-6 in which carbonyl groups and UPy motifs can reconfigurably anchor to water molecules in the nano-confined space due to strong and abundant hydrogen bonding interactions. To confirm our hypothesis, XPS was performed with the atomic weight percent of the constituent elements shown (Fig. 3h). The broad XPS spectrum showed that the percentages of O1s and N1s on the rear surface were greater than those on the top surface, respectively. Moreover, the fine spectra of O1s (O=C and O-C) and N1s (N-C and N=C) persisted on both sides of the NCC membrane (Supplementary Fig. S20 and Supplementary Table S2). Compared to those on the top surface, the percentages of O-C (12.2%) and N-C (19.5%) on the rear surface of NCC membrane were greater, and the percentages of C-C and C-H in C1s were lower. The Janus wetting properties and chemical heterogeneity of the two sides of the NCC membrane were also verified by zeta potential measurement (Supplementary Fig. S21). As the pH increased, the surface charge on the rear side became more negative than that on the top side. On the one hand, carbonyl groups and UPy motifs on the rear side can engage in hydrogen bonding or electrostatic interactions, leading to charge redistribution or the formation of charged species^{28,29}. On the other hand, when the pH shifts towards basic conditions, the carbonyl and UPy units become more deprotonated³⁰. This deprotonation process leads to a reduction in the positive charge or even the generation of a notable negative charge. These results indicated that more polar groups were located at the rear surface due to the chemical configurations of the nano-confined space. A high density of interfacial hydrogen bonding interactions can enhance the entropy barrier and reduce the crystallization rates of Tetra-PCL-UPy chains at the rear side, thus enabling a heterogeneous crystallization of the resultant NCC nano-film.

Reverse osmosis desalination performance

The reverse osmosis (RO) desalination capabilities were examined. It is noted that a linear relationship between the pure water flux and hydraulic pressures was observed in the range of 2–60 bar (Supplementary Fig. S22), indicating the mechanical robustness and stability

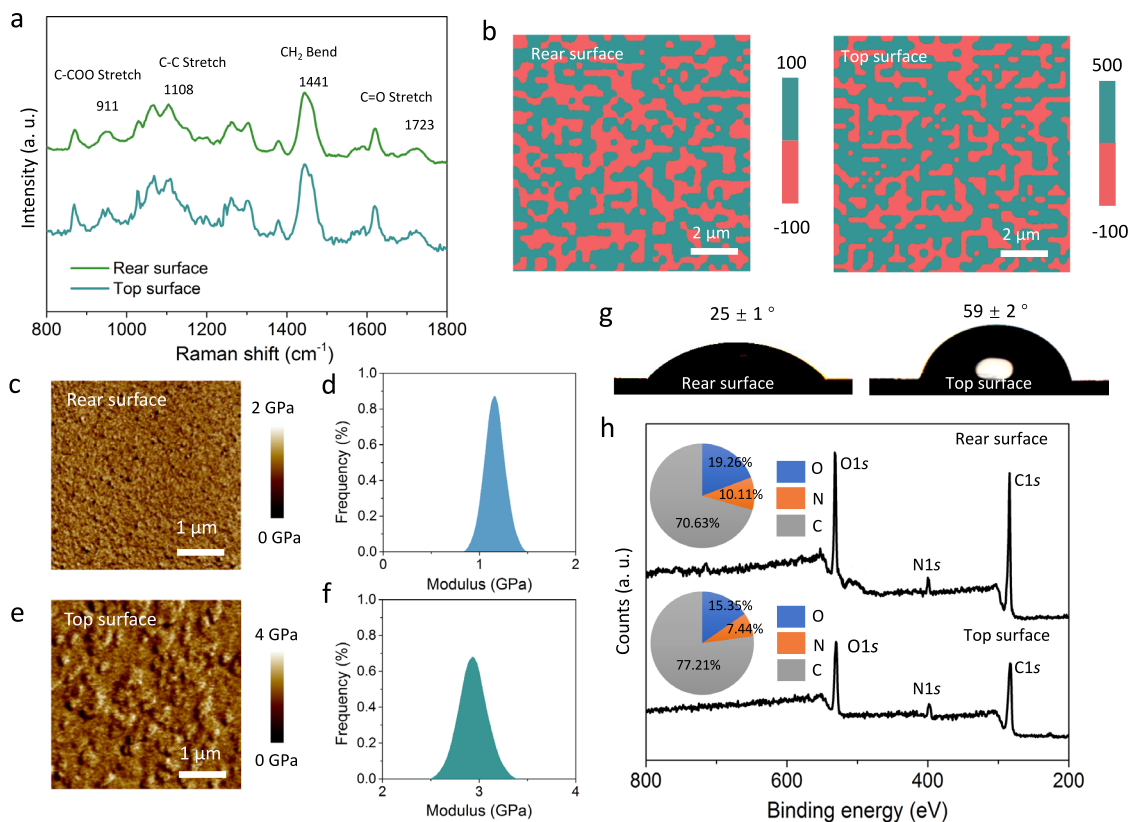


Fig. 3 | Controllable crystallization and Janus surfaces of the NCC membrane. Raman spectra (a) and mapping (b) of the two sides of the NCC-6 membrane. Modulus images and distributions of the rear (c, d) and top (e, f) surfaces of the NCC-6

membrane, as measured by AFM based indentation. g WCAs of the two sides of the NCC-6 membrane. h Surface XPS spectrum of the two sides of the NCC-6 membrane. Error bars represent the standard deviation from three duplicate experiments.

of the NCC-6 membrane. The water flux and solute rejection of the resultant membranes were tested at 10 bar pressure with 1000 ppm salt solutions including NaCl, KCl, CaCl₂, MgCl₂, AlCl₃ (Fig. 4 and Supplementary Tables S3, 4). For all the tested salt solutions, the NCC-6 membrane displayed a water flux of more than 100 L m⁻² h⁻¹, which was 1.15–1.3 times greater than the NRC-6 membrane (Fig. 4a). As shown in Fig. 4b, the NCC-6 membrane exhibited -99.2% rejection rate for monovalent ions, greatly outperforming the NRC-6 membrane of -70% for the KCl and NaCl solution, respectively. In addition, NCC-6 showed a more than 99.5% removal for divalent ion solutions and a 99.7% rejection rate for a AlCl₃ solution. Moreover, NCC-12 and NCC-18 exhibited reduced water flux and enhanced salt rejection when compared to the NCC-6 membrane (Supplementary Fig. S23). We further evaluated the water/solute selectivity, defined as the value of A/B, where A and B are water and solute permeability coefficient, respectively. As the thickness of the NCC membranes increased, the water permeability coefficient (water permeance) first witnessed a sharp reduction and then slightly decreased, at an external pressure of 10 bar (Supplementary Fig. S24). The water permeance of the NCC-6 membrane reached 14.8 L m⁻² h⁻¹ bar⁻¹, which was nearly 1.5 times that of NCC-12 and more than twice that of NCC-18, while the NaCl permeability coefficient decreased from 0.27 to 0.16 L m⁻² h⁻¹, for the NCC-6, NCC-12, and NCC-18 membranes, driven by a 10-bar pressure with 1000 ppm NaCl solution (Fig. 4c and Supplementary Table S4). We subsequently calculated the water/solute selectivity of the NCC and NRC membranes (Supplementary Tables S3, 4). The NCC-6 membrane demonstrated a water/NaCl selectivity exceeding 54 bar⁻¹ (Fig. 4d), which is greater than NCC-12 (42.5 bar⁻¹) and NCC-18 (45.6 bar⁻¹). As indicated in Fig. 4e, the NCC-6 membrane demonstrated a high water permeance (14.8 L m⁻² h⁻¹ bar⁻¹) and an extraordinary water/NaCl selectivity (54 bar⁻¹) when tested with a 1000 ppm NaCl solution at

10 bar at room temperature of approximately 25 °C, outperforming the upper bound of water/NaCl selectivity observed in the current state-of-the-art RO and NF membranes^{16,31–33}. Notably, NCC-6 was more than 55 times that of NRC-6 in water/NaCl selectivity at same tested conditions (Supplementary Fig. S25 and Supplementary Table S3). In addition, the NCC-6 membrane showed a water/CaCl₂ or water/MgCl₂ selectivity of over 90 bar⁻¹, and a water/AlCl₃ selectivity exceeding 150 bar⁻¹. Surprisingly, the water/AlCl₃ selectivity of the NCC-18 membrane can approach 250 bar⁻¹ (Supplementary Table S4). Therefore, the NCC-6 membrane exhibited improved water permeance and water/salt selectivity, which is primarily due to the improved fractional free volume and narrowed pore size distribution. Long-term RO separation measurements were conducted with a feed solution of 1000 ppm NaCl and an applied pressure of 10 bar (Fig. 4f). The NCC-6 membrane maintained a high NaCl rejection rate over 99% for the initial 120-h operation and reached 98.6% with a total duration of 168 h, while the water flux slightly decreased by 8.3%, possibly due to concentration polarization. The morphological and structural stability of NCC-6 after 7-days of separation were confirmed by SEM, AFM, and XRD measurements (Supplementary Figs. S26–28). The RO separation performance of NaCl solutions with high concentrations was also studied (Supplementary Fig. S29). As the NaCl concentration increased to 5000 ppm, both the water flux and the rejection rates of the NCC-6 membrane slightly decreased. Notably, at a NaCl concentration of 3000 ppm, the rejection rate remained over 99% and the water flux reached over 125 L m⁻² h⁻¹.

We also evaluated the boron removal capabilities of the NCC-6 and NRC-6 membranes driven by the hydraulic pressure at 10 bar. The feed solution consisted of boric acid (H₃BO₃) at a concentration of 5 ppm, and NaOH was used to adjust the pH. As shown in Supplementary Fig. S30a, for the neutral H₃BO₃ molecule at pH=7, the NCC-6

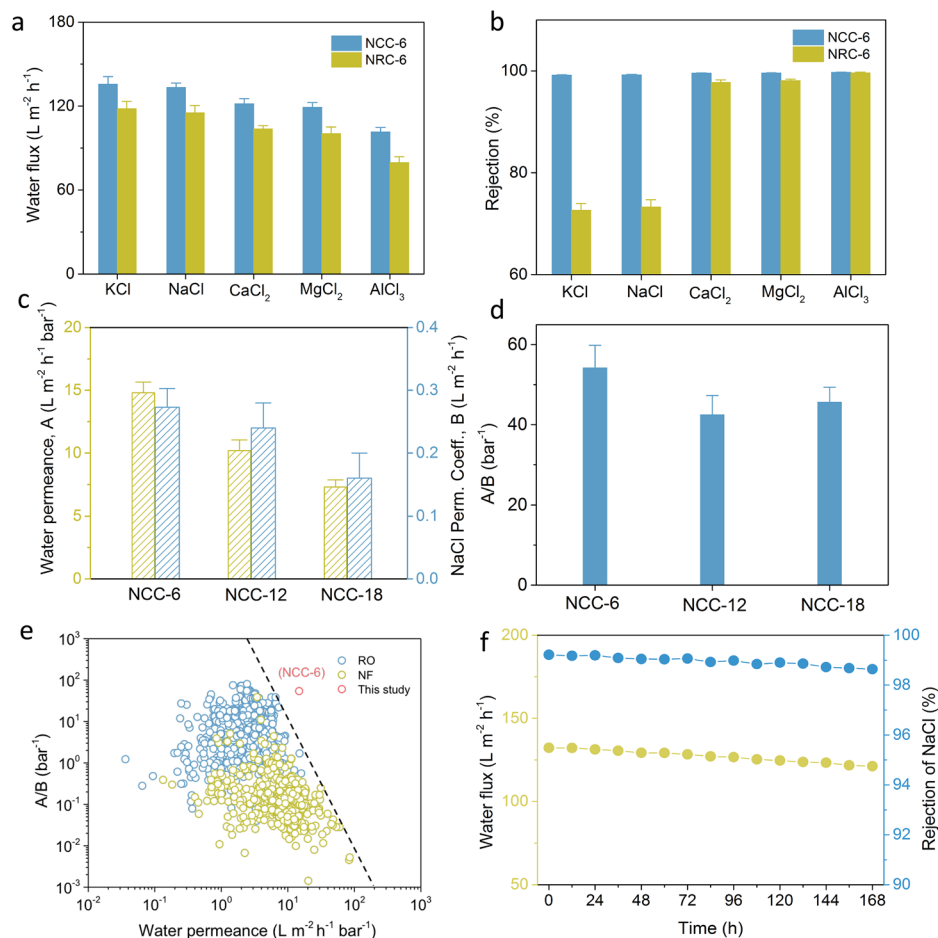


Fig. 4 | Desalination performance. Water flux (a) and single salt rejection (b) of the NCC-6 membrane and the NRC-6 membrane. The experimental conditions are as follows: an effective membrane area of 3 cm², a 1000 ppm salt feed solution, a crossflow velocity of 50 L h⁻¹, and a constant pressure of 10 bar. c Water permeance, A and NaCl permeability coefficient, B of the NCC-6, NCC-12, and NCC-18

membranes. d The water/NaCl selectivity of the NCC-6, NCC-12, and NCC-18 membranes. e The comparison of water permeance and water/NaCl selectivity with the literature reported reverse osmosis polymer membranes. f Water flux and salt rejection of 1000 ppm NaCl solution at 10-bar and 168-h desalination. Error bars represent the standard deviation from three duplicate experiments.

membrane exhibited a rejection rate of ~75%, which is greater than the NRC-6 membrane. The boron rejection rate increased when tested at basic conditions, for example, the boron rejection exceeded 98% for the anionic B(OH)₄⁻ at pH=10. Moreover, at neutral condition, the boron removal rate of NCC-12 and NCC-18 rose to 88.5% and 93.4%, respectively (Supplementary Fig. S30b). Therefore, the NCC-6 membrane showed a significant advantage in terms of boron removal under the same conditions.

The chlorine resistant measurement of the NCC-6 and NRC-6 membranes was investigated (Supplementary Fig. S31). The membrane was immersed in a 200 ppm NaClO solution under continuous stirring for 24 h, and the total chlorine exposure was 4800 ppm h. The pH values of the NaClO solution was adjusted to 5, 7, and 9, respectively. Even at high pH levels, the water permeance and NaCl rejection rates of the NCC-6 and NRC-6 membranes remained largely unaffected, indicating their excellent chlorine resistance. We further evaluated the structural and desalination stability of the NCC-6 membrane when soaked in acidic (pH=3), basic (pH=11), and urea (1 wt%) aqueous solutions for 24 h, respectively. As indicated in SEM measurements (Supplementary Fig. S32), the NCC-6 membranes remained defect-free under these three measurements. XRD analysis indicated that the crystalline profiles of the NCC-6 membranes remained unchanged under these treated conditions (Supplementary Fig. S33). Besides, the RO desalination performance did not show noticeable changes at 1000 ppm NaCl solution and a 10-bar pressure (Supplementary Fig. S34). To

further elucidate the membrane stability at the actual operational conditions, we performed the in-situ roughness studies on the NCC-6 membrane that were soaked in DI water and 1M NaCl solution, respectively (Supplementary Fig. S35). The surface roughness showed no significant variations of in both conditions, in contrast to the measurements at air condition (Fig. 2c).

These combinational properties highlight the significant advantages of the NCC-6 membranes over the NRC-6 membrane in terms of excellent resistance to harsh conditions (acid, base, hydrogen-bonding competitor solution, and chlorine), excellent RO desalination to salt solutions and boron, sustained solute removal, and structural stability, which underscores the importance of molecular engineering, interfacial chemistry, and controllable crystallization in the fabrication of ultrathin membranes for high-performance desalination.

Mechanisms elucidated by molecular dynamics simulation

Using molecular dynamics (MD) simulations, we elucidated the impact of molecular design and nano-confinement on the microstructures and pore sizes of the membranes. Figure 5a and Supplementary Fig. S36 showed the equilibrium configurations of tetra-oligomers with distinct end-functional groups. Two sandwich models were established to simulate the interactions between tetra-PCL-OH or tetra-PCL-UPy and water molecules (Fig. 5b and Supplementary Fig. S37). Once the tetra-oligomers/water simulation system reached an equilibrium state, we extracted the structures of tetra-oligomers for subsequent density

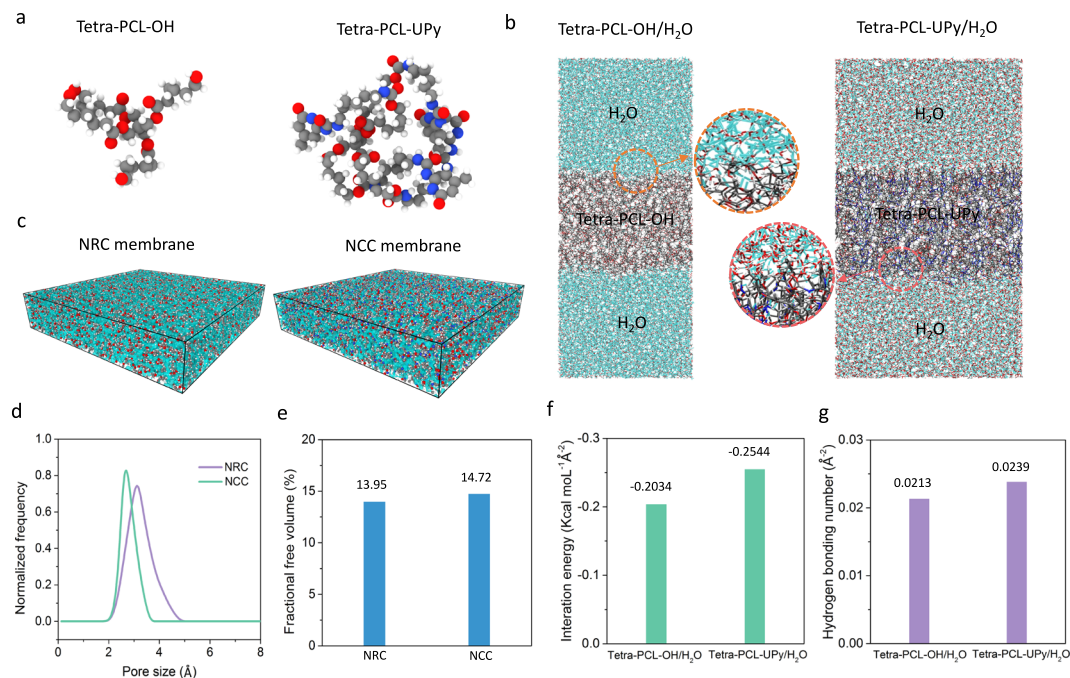


Fig. 5 | Molecular dynamics simulation. **a** Molecular structures of tetra-PCL-OH and tetra-PCL-UPy. **b** Sandwich models for computing the interactions between tetra-PCL-OH or tetra-PCL-UPy and water molecules, where cyan lines represent the hydrogen bonds formed in the simulation system. **c** Free volume in NRC and NCC (see the space occupied by translucent light green volume) detected by a

theoretical probe with a radius of 1 Å. Simulated pore size distributions (**d**) and fractional free volume (**e**) of NRC and NCC. **f** Areal density of the interaction energy between tetra-PCL-OH or tetra-PCL-UPy and water molecules. **g** Areal density of hydrogen bonds formed between tetra-PCL-OH or tetra-PCL-UPy and water molecules.

calculations and voids analysis. As illustrated in Fig. 5c and Supplementary Fig. S38, the two structural models demonstrated the free volume in Tetra-PCL-OH and Tetra-PCL-UPy (see the space occupied by translucent light green volume) detected by a theoretical probe with a radius of 1 Å. The simulated pore size distributions were calculated based on the constructed models. In contrast to the NRC membrane derived from tetra-PCL-OH, the NCC membrane obtained from tetra-PCL-UPy exhibited a high density of smaller pore sizes, as evidenced by the narrower distribution of pore sizes (Fig. 5d) and the higher fractional free volume (Fig. 5e). These findings are consistent with the experimental observations that the organized assembly of Tetra-PCL-UPy and the controllable crystallization reduce the pore sizes and narrow the pore distributions (Supplementary Fig. S16). Such structures of the NCC membrane are greatly advantageous for promoting water flux and reducing ions flux. We noted that the simulated pore sizes of both the NCC membrane and NRC membrane are slightly greater than those of H₂O molecules (2.7 Å) but smaller than the hydrated monovalent (K⁺: 6.62 Å; Na⁺: 7.16 Å) and multivalent (Mg²⁺: 8.56 Å; Ca²⁺: 8.24; Al³⁺: 9.5 Å) ions, thus confirming the observations of the water flux, ions rejections, and water/ions selectivity of the NCC-6 membrane.

We also investigated the interfacial interaction energy between tetra-oligomers and water molecules (Fig. 5b and Supplementary Fig. S36). After MD relaxation, we found that the interfacial energy between tetra-PCL-UPy and water molecules (0.2544 kcal mol⁻¹ Å⁻²) was greater than that between tetra-PCL-OH and water molecules (0.2034 kcal mol⁻¹ Å⁻²) (Fig. 5f), indicating strong attractive interactions between tetra-PCL-UPy and H₂O. Moreover, a large number of UPy motifs accumulate at the air/water interface under nano-confinement. To further elucidate the effect of interfacial hydrogen bonding on the formation of controllable and organized crystallizations in the nano-films, we quantified the number of hydrogen bonds at the nano-confined interface of tetra-PCL-OH/H₂O and tetra-PCL-UPy/H₂O. More hydrogen bonds were established at the interface

between tetra-PCL-UPy and water molecules, as shown in Fig. 5g. These results confirm that a large quantity of polar functional groups accumulate near the water interface due to strong hydrogen bonding interactions with water molecules, particularly UPy motifs, which form stronger hydrogen bonding interactions than both hydroxyl and carbonyl units at the air/water interface, significantly lowering the conformation entropy and enabling controllable crystallization within the NCC-series membranes.

Discussion

We developed high-performance reverse osmosis membranes by meticulously managing the alignment and crystallization of UPy-ended amphiphilic oligomers at nano-confined air/water interface. The hydrophobic PCL chains ending with UPy segments naturally adjust and set their molecular configuration at air/water interfaces due to strong multivalent H-bond interactions. When these oligomer chains maintain a consistent orientation at the nanoscale, they undergo crystallization throughout the membrane, promoting a uniform distribution of pore size, which in turn boosts the water/solute selectivity. On the other hand, the powerful bonding of the UPy terminations restricts polymer chain movement, resulting in controllable crystallization and surfaces heterogeneity of the membrane. This increases the free volume proportion and augments water permeation. Notably, the NCC-6 membrane exhibits a pure water permeability of 14.8 L m⁻² h⁻¹ bar⁻¹ and a water/NaCl selectivity of over 54 bar⁻¹, which surpass the upper bound of water/NaCl selectivity of the state-of-the-art polyamide membranes.

However, we acknowledge the limitations of the current NCC membrane design, particularly the absence of covalent crosslinking, which raises concerns regarding their stability under harsh conditions. The non-covalent bonding and self-assembly mechanisms render the membranes susceptible to breakdown at elevated temperatures, exposure to solvents, and interactions with surfactants. These limitations highlight the need for further advancements to enhance their thermal and chemical stability. Future work will focus on exploring

strategies such as noncovalent/covalent crosslinking, the incorporation of stabilizing additives, or the development of hybrid materials to address these challenges. In addition, future studies will prioritize standardized testing protocols under consistent conditions to provide a more accurate and reliable comparison of membrane selectivity and permeability. This will help address the limitations of our current comparative analysis and provide a stronger foundation for evaluating the performance of NCC membranes relative to existing technologies.

Looking forward, our discoveries not only deepen the understanding of the relationships among the structure, properties, and performance in desalination membranes but also introduce a concept for guiding the design of supramolecular polymeric membranes using precise self-assembly and controllable crystallization to achieve optimal desalination outcomes. Moreover, this approach aligns well with existing membrane technologies, laying the foundation for holistic enhancements in modern polymer membrane systems. We anticipate that as this concept matures, manufacturing techniques will evolve to accommodate various membrane-related applications, such as osmotic energy conversion and wastewater treatment.

Methods

Materials and methods

ϵ -Caprolactone (ϵ -CL), stannous isoocanoate, pentaerythritol, dibutyltin dilaurate (DBTL), AlCl_3 ($\geq 99\%$), MgCl_2 ($\geq 99.99\%$), CaCl_2 ($\geq 97\%$), KCl ($\geq 99\%$), and NaCl ($\geq 99\%$) were purchased from J&K Scientific. Analytical grade boric acid $\text{B}(\text{OH})_3$ was obtained from Sigma-Aldrich. 2-amino-4-hydroxy-6-methylpyrimidine 99% was purchased from Acros Organics. All chemicals and solvents were used as received. Single crystal silicon wafers were purchased from Si-Mat Germany and used as a substrate for atomic force microscopy (AFM) measurements.

Synthesis of tetra-oligomers polycaprolactone (PCL)

The tetra-oligomer PCL was synthesized by ring-opening polymerization of ϵ -caprolactone (ϵ -CL)³⁴. Pentaerythritol (initiator, 0.1362 g), ϵ -CL (10 g), and stannous isoocanoate (catalyst, 0.3 wt%) were added into a 50-mL flask. The reaction was conducted at 120 °C for 10 h under an argon atmosphere. The product was dissolved in toluene and precipitated in cold methanol, and then vacuum-dried overnight.

Synthesis of 2-(6-isocyanato-hexylamino)-6-methyl-4[1H]-pyrimidinone (UPy-NCO)

2-(6-Isocyanato-hexylamino)-6-methyl-4[1H]-pyrimidinone (UPy-NCO) was prepared using a literature procedure from Meijer³⁵. 2-Amino-4-hydroxy-6-methylpyrimidine (10 g, 79.9 mmol) was added to a 250 mL round bottomed flask. Hexamethylene diisocyanate (HMDI, 100 mL, 624 mmol) and pyridine (7 mL) were then added, the flask was fitted with a reflux condenser, and the mixture was stirred at 100 °C overnight under dry nitrogen. Pentane (30 mL) was then added and the solid product was collected by filtration. The white powder was washed 3 times with 125 mL portions of acetone to remove unreacted HMDI and then dried overnight under high vacuum at 60 °C (yield 95%).

Synthesis of Tetra-PCL-UPy

Tetra-oligomer PCL (1 mmol) and UPy-NCO (4 mmol) were added into DMF solution (50 mL) and stirred at 50 °C until the solid was dissolved. Subsequently, six drops of dibutyltin dilaurate (DBTL) were added into the solution. The reaction was kept at 50 °C for 20 h. The polymer was obtained by precipitation in cold ether. The polymer was re-dissolved in toluene and re-precipitated in cold ether three times. The final product was obtained by overnight vacuum drying at 40 °C.

Preparation of ultrathin crystalline nanofilms

First, tetra-oligomer PCL powder was dissolved in CHCl_3 to prepare different concentrations of polymer solution (2–10 mg mL^{-1}). Then,

5 μL of the polymer solution is gently dropped onto the water surface, which rapidly spread. An ultrathin membrane was formed at the nanoconfined space in several seconds and then was transferred to various supports such as polyethersulfone (PES) and silicon wafers for desalination process and characterization.

General characterizations

^1H (400 MHz) NMR spectra were recorded on a Bruker DRX 400 spectrometer in chloroform- d . Thermogravimetric analysis (TGA) was conducted under N_2 in the range of 30–600 °C with a heating rate of 10 °C min^{-1} . Gel permeation chromatography (GPC) was conducted using an Agilent Technologies 1260 Infinity, and the data were processed using Agilent GPC/SEC software, polystyrene was used as the calibrant. Samples for GPC analysis were dissolved in analytical grade THF (2 mg mL^{-1}). DSC measurements were performed under N_2 using an MDSC 2910 system operating at a heating/cooling rate of 10 °C min^{-1} in the range of –40 to 110 °C, unless indicated otherwise. Data from the second heating cycle and the reverse heat flow curve are reported unless indicated otherwise. Fourier transform infrared (FT-IR) spectra were recorded using a Fourier transform infrared spectrometer (PE Spectrum 100) for wavelengths ranging from 400 to 4000 cm^{-1} . The static contact angle of the nanofilms and surface tension of the microdroplets were determined with OCA20 equipment (Data Physics, Germany). A digital camera was used to monitor the shape of the droplet immediately after the droplet deposition. Each experiment data was independently performed for three times. The structures of the nanofilms were examined by using grazing incidence X-ray diffraction (GIXRD) (Malvern Panalytical's X'Pert³). The nanofilm was exposed to X-ray for 5 min with an incidence angle of 0.12°. The orientations of the polymer chains were tested by grazing incidence wide-angle X-ray scattering (GI-WAXS) (XEUS). Raman mapping and spectra were recorded on a WITec alpha300 instrument at a wavelength of 532 nm to detect the characteristic peaks of the crystalline nanofilms from the tetra-oligomer PCL and to determine the characteristic peaks intensity and the distribution of the crystalline and amorphous domains. The surface roughness and thickness of the nanofilms were measured by atomic force microscopy (AFM; Bruker Dimension Icon with ScanAsyst). The free-standing nanofilms were transferred to silicon wafers and dried. The surface roughness is presented as the root-mean-square roughness (R_{rms}). The nanofilm thickness was measured from the distance from the silicon layer to the nanofilm. The chemical composition and elemental composition of the nanofilms were analyzed by X-ray photoelectron spectroscopy (XPS; PHI Model 5802), and the angle-resolved technique was adopted. Transmission electronic microscope (TEM; FEI/Philips Tecnai 12 BioTWIN) was used to study the morphology of the nanofilms. Freestanding nanofilms were transferred onto copper grids for TEM imaging. The surface images of the nanofilms were characterized by high resolution scanning electron microscopy (SEM; FEI Quanta 450) with an accelerating voltage of 5 kV. The crystalline morphology of the nanofilm was observed with a polarizing optical microscope (POM; Olympus BH2-UMA) equipped with a camera (Olympus DP11).

Zeta potential measurement at the membrane surface

The zeta potential of the membrane surface was measured by a Malvern type Zetasizer Nano ZSP. A rectangular clamp cell was used to fix the membrane samples. For each test, a membrane sheet (1 \times 2 cm^2) was cut and attached onto a holder with water-proof double-sided tape, after which the holder was fixed to the rectangular clamp cell. The system was washed with DI water prior to each test. The pH and conductivity were calibrated before each test. The 50 mM HCl and NaOH solutions were titrated from pH 3 to 10, and the zeta potential of the surface was measured.

Young's modulus measurement by peak force quantitative nanomechanical mapping (PFQNM) method

The modulus measurements were performed in PFQNM mode^{36,37} on a Dimension Icon AFM system (Bruker Dimension Icon with ScanAsyst). Images were collected with Si₃N₄ tips (DNP-B, Bruker) at a 1.0 Hz scan rate. The spring constant was calibrated by the thermal tuning method. This mode was based on peak force tapping, which involved generating a very fast force curve at every pixel in the image by modulating the Z piezo at -1 kHz with an amplitude of 200 nm. The peak force of each of these curves was then used as the imaging feedback signal. Analysis of the force curve data was performed in real-time, providing a map of multiple mechanical properties, such as the modulus and adhesion, which had a similar resolution to that of the height image. This mode controlled the tip/sample interaction directly to decrease the deformation of the sample and the contact area, so minimal damage to the probe or sample occurred and a higher resolution was acquired.

Wide-angle X-ray diffraction

To determine the degree of crystallinity (X_c), the WAXD profile at 2 Theta = 20–25 degrees was fitted by the separate reflection peaks of crystals and the amorphous halo. X_c was calculated by the following Eq. (1):

$$X_c = \frac{A_c}{A_c + A_a} \times 100\% \quad (1)$$

where A_a represents the area under the amorphous halo and A_c is the area of the crystalline peaks in the WAXD profile.

Evaluation of membrane desalination performance in Reverse Osmosis (RO)

The desalination performance of the nanofilms was evaluated in a filtration setup with a cross-flow filtration configuration. The temperature was maintained at 25 (±1) °C. The feed solution, approximately 10 L in volume, was pumped from a feed tank using a high-pressure diaphragm pump into the membrane cell. The samples were first conditioned for a minimum of 8 h under a pressure of 10 bar using pure water to achieve a steady-state conditions. The effective area of the membranes used in the cell was 3 cm². The cross-flow velocity was 50 L h⁻¹, and the applied pressure was 10 bar. The feed concentration of salts (NaCl, KCl, CaCl₂, MgCl₂, AlCl₃) was 1000 ppm. For the boron rejection, the concentration in the feed solution was 5 ppm, and NaOH was used to adjust the pH of the solution. The solute concentrations in the feed and the permeate were monitored by a conductivity meter and an inductively coupled plasma optical emission spectrometry (ICP-OES). The water-salt selectivity is defined as $\alpha \equiv A/B$, where A and B are water and salt permeability, respectively. Water permeability is presented in the unit of L m⁻² h⁻¹ bar⁻¹. Salt permeability is presented in the unit of L m⁻² h^{-1.38-40}. At least four membrane coupons were tested to obtain an average value and standard deviation.

The water flux, J_w (L m⁻² h⁻¹), was calculated using the following Eq. (2):

$$J_w = \frac{\Delta V}{A t} \quad (2)$$

where ΔV is the permeate water volume (L) collected over the period t (h), and A is the effective membrane area (m²), respectively.

The water permeability coefficient, also called pure water permeance, A (L m⁻² h⁻¹ bar⁻¹), was calculated using the following Eq. (3):

$$A = \frac{\Delta V}{A t \Delta P} \quad (3)$$

where ΔV is the permeate water volume (L) collected over the period of time (h), A is the effective membrane area (m²), and ΔP is the transmembrane pressure (bar), respectively.

The observed salt rejection, R , was calculated using the following Eq. (4):

$$R = \left(1 - \frac{C_p}{C_f}\right) \times 100\% \quad (4)$$

where R is the salt rejection (%), and C_p and C_f are the salt concentrations of the permeate and feed solution, respectively.

Considering the concentration polarization, the salt permeability coefficient, B (L m⁻² h⁻¹), was calculated using the following Eq. (5):

$$B = J_w \left(\frac{1-R}{R}\right) e^{\left(-\frac{J_w}{k}\right)} \quad (5)$$

where k is the feed channel mass transfer coefficient, estimated from the cell geometry and the crossflow rate.

Chlorine-resistant measurement

The nanofilms were soaked in a 200 ppm NaClO solution under continuous stirring for 24 h. The pH of NaClO was adjusted to 5.0, 7.0, and 9.0, using hydrogen chlorine and sodium hydroxide solutions. The container was wrapped with tin foil and stored in a dark environment. After being removed from the NaClO solution, the membrane was thoroughly cleaned with DI water before conducting desalination experiments.

Data availability

The data supporting the findings of this study are available within the Article and its Supplementary Information. All data are available from the corresponding author upon request.

Code availability

The simulation codes used in this study are available from the corresponding authors on request.

References

- Park, H. B., Kamcev, J., Robeson, L. M., Elimelech, M. & Freeman, B. D. Maximizing the right stuff: The trade-off between membrane permeability and selectivity. *Science* **356**, 1137 (2017).
- Yang, Z., Long, L., Wu, C. & Tang, C. Y. High permeance or high selectivity? Optimization of system-scale nanofiltration performance constrained by the upper bound. *ACS EST Eng.* **2**, 377–390 (2021).
- Werber, J. R., Osuji, C. O. & Elimelech, M. Materials for next-generation desalination and water purification membranes. *Nat. Rev. Mater.* **1**, 1–15 (2016).
- Sujanani, R. et al. Designing solute-tailored selectivity in membranes: Perspectives for water reuse and resource recovery. *ACS Macro Lett.* **9**, 1709–1717 (2020).
- Epsztein, R., DuChanois, R. M., Ritt, C. L., Noy, A. & Elimelech, M. Towards single-species selectivity of membranes with subnanometre pores. *Nat. Nanotech.* **15**, 426–436 (2020).
- Culp, T. E. et al. Nanoscale control of internal inhomogeneity enhances water transport in desalination membranes. *Science* **371**, 72–75 (2021).
- Freger, V. Nanoscale heterogeneity of polyamide membranes formed by interfacial polymerization. *Langmuir* **19**, 4791–4797 (2003).
- Kim, S. H., Kwak, S.-Y. & Suzuki, T. Positron annihilation spectroscopic evidence to demonstrate the flux-enhancement mechanism in morphology-controlled thin-film-composite (TFC) membrane. *Environ. Sci. Tech.* **39**, 1764–1770 (2005).
- Kim, S.-J. et al. Characterization of pore size distribution (PSD) in cellulose triacetate (CTA) and polyamide (PA) thin active layers by

- positron annihilation lifetime spectroscopy (PALS) and fractional rejection (FR) method. *J. Membr. Sci.* **527**, 143–151 (2017).
10. Zhao, G., Gao, H., Qu, Z., Fan, H. & Meng, H. Anhydrous interfacial polymerization of sub-1 Å sieving polyamide membrane. *Nat. Commun.* **14**, 7624 (2023).
 11. Sarkar, P., Modak, S. & Karan, S. Ultraselective and highly permeable polyamide nanofilms for ionic and molecular nanofiltration. *Adv. Funct. Mater.* **31**, 2007054 (2021).
 12. Shen, L. et al. Polyamide-based membranes with structural homogeneity for ultrafast molecular sieving. *Nat. Commun.* **13**, 500 (2022).
 13. Liang, Y. et al. Polyamide nanofiltration membrane with highly uniform sub-nanometre pores for sub-1 Å precision separation. *Nat. Commun.* **11**, 2015 (2020).
 14. Bai, Y. et al. Microstructure optimization of bioderived polyester nanofilms for antibiotic desalination via nanofiltration. *Sci. Adv.* **9**, eadg6134 (2023).
 15. Jiang, Z. et al. Aligned macrocycle pores in ultrathin films for accurate molecular sieving. *Nature* **609**, 58–64 (2022).
 16. Di Vincenzo, M. et al. Tunable membranes incorporating artificial water channels for high-performance brackish/low-salinity water reverse osmosis desalination. *Proc. Natl. Acad. Sci. USA* **118**, e2022200118 (2021).
 17. Lu, X. et al. Tuning the permselectivity of polymeric desalination membranes via control of polymer crystallite size. *Nat. Commun.* **10**, 2347 (2019).
 18. Huang, J. et al. Polymeric membranes with highly homogenized nanopores for ultrafast water purification. *Nat. Sustain.* **7**, 901–909 (2024).
 19. Yao, Y. et al. More resilient polyester membranes for high-performance reverse osmosis desalination. *Science* **384**, 333–338 (2024).
 20. Zuo, P. et al. Near-frictionless ion transport within triazine framework membranes. *Nature* **617**, 299–305 (2023).
 21. Lu, G., Zhu, Q., Ma, R., He, W. & Wu, J. Tough Yet Reversible Hydrogel Adhesives with Cooperative Energy Dissipation for Multifunctional Wearable Sensors. *Adv. Funct. Mater.* **33**, 2306914 (2023).
 22. Zhao, Y. et al. Diurnal humidity cycle driven selective ion transport across clustered polycation membrane. *Nat. Commun.* **15**, 7161 (2024).
 23. Lu, G. et al. High-Performance Supramolecular Organogel Adhesives for Antimicrobial Applications in Diverse Conditions. *ACS Appl. Mater. Interfaces* **15**, 44194–44204 (2023).
 24. Tadmor, R. & Pepper, K. G. Interfacial tension and spreading coefficient for thin films. *Langmuir* **24**, 3185–3190 (2008).
 25. Harkins, W. D. & Feldman, A. Films. The spreading of liquids and the spreading coefficient. *J. Am. Chem. Soc.* **44**, 2665–2685 (1922).
 26. Lacoste, T., Huser, T., Prioli, R. & Heinzlmann, H. Contrast enhancement using polarization-modulation scanning near-field optical microscopy (PM-SNOM). *Ultramicroscopy* **71**, 333–340 (1998).
 27. Lin, S.-S., Yemelyanov, K. M., Pugh, E. N. Jr & Engheta, N. Separation and contrast enhancement of overlapping cast shadow components using polarization. *Opt. Express* **14**, 7099–7108 (2006).
 28. Ohto, T. et al. Lipid carbonyl groups terminate the hydrogen bond network of membrane-bound water. *J. Phys. Chem. Lett.* **6**, 4499–4503 (2015).
 29. Bartlett, G. J., Newberry, R. W., VanVeller, B., Raines, R. T. & Woolfson, D. N. Interplay of hydrogen bonds and $n \rightarrow \pi^*$ interactions in proteins. *J. Am. Chem. Soc.* **135**, 18682–18688 (2013).
 30. Yu, G., Jie, K. & Huang, F. Supramolecular amphiphiles based on host–guest molecular recognition motifs. *Chem. Rev.* **115**, 7240–7303 (2015).
 31. Yang, Z., Guo, H. & Tang, C. Y. The upper bound of thin-film composite (TFC) polyamide membranes for desalination. *J. Membr. Sci.* **590**, 117297 (2019).
 32. Di Vincenzo, M. et al. Biomimetic artificial water channel membranes for enhanced desalination. *Nat. Nanotechnol.* **16**, 190–196 (2021).
 33. Wen, Y. et al. Metal-organic framework enables ultraselective polyamide membrane for desalination and water reuse. *Sci. Adv.* **8**, eabm4149 (2022).
 34. Jin, B. et al. Programming a crystalline shape memory polymer network with thermo- and photo-reversible bonds toward a single-component soft robot. *Sci. Adv.* **4**, eaao3865 (2018).
 35. Sijbesma, R. P. et al. Reversible polymers formed from self-complementary monomers using quadruple hydrogen bonding. *Science* **278**, 1601–1604 (1997).
 36. Liang, B. et al. Microporous membranes comprising conjugated polymers with rigid backbones enable ultrafast organic-solvent nanofiltration. *Nat. Chem.* **10**, 961–967 (2018).
 37. Lu, G. et al. Nano-confined Supramolecular Assembly of Ultrathin Crystalline Polymer Membranes for High-Performance Nanofiltration. *Adv. Funct. Mater.* **34**, 2309913 (2024).
 38. Werber, J. R., Deshmukh, A. & Elimelech, M. The critical need for increased selectivity, not increased water permeability, for desalination membranes. *Environ. Sci. Tech. Lett.* **3**, 112–120 (2016).
 39. Geise, G. M., Paul, D. R. & Freeman, B. D. Fundamental water and salt transport properties of polymeric materials. *Prog. Polym. Sci.* **39**, 1–42 (2014).
 40. Chen, X., Boo, C. & Yip, N. Y. Influence of solute molecular diameter on permeability-selectivity tradeoff of thin-film composite polyamide membranes in aqueous separations. *Water Res.* **201**, 117311 (2021).

Acknowledgements

This work was supported by RGC Theme-based Research Scheme (T21-604/19-R) (A.K.A.), RGC Research Fellow Scheme (RFS2223-1S04) (A.K.A.), Hong Kong Innovation and Technology Commission (PRP/077/22FX) (A.K.A.) University of Hong Kong (2201100473) (S.Z.), National Natural Science Foundation of China (22205145) (B.D.), One Hundred-Talent Plan of Chinese Academy of Sciences (Y610061033) (J.W.), and Two-Hundred Talents Plan of Yantai (Y739011021) (J.W.).

Author contributions

G.L. conceived the concept, designed experiments, and drafted the manuscript. G.L., Y.Y.Z., W.S., J.S., and B.D. conducted experiments and characterizations. H.A. performed MD calculations. H.X., Y.Z., and J.W. contributed to the discussion of data. G.L., S.Z., A.K.A., B.V.B., R.D., X.C., and H.Z. revised the manuscript. G.L., H.A., and Y.Y.Z. contributed equally to this work. S.Z., G.L., and A.K.A. supervised this project.

Competing interests

The authors declare no competing interests.

Additional information

Supplementary information The online version contains supplementary material available at <https://doi.org/10.1038/s41467-025-57353-0>.

Correspondence and requests for materials should be addressed to Gang Lu, Alicia Kyoungjin An or Shuang Zheng.

Peer review information *Nature Communications* thanks Anthony Straub and the other, anonymous, reviewer(s) for their contribution to the peer review of this work. A peer review file is available.

Reprints and permissions information is available at <http://www.nature.com/reprints>

Publisher's note Springer Nature remains neutral with regard to jurisdictional claims in published maps and institutional affiliations.

Open Access This article is licensed under a Creative Commons Attribution-NonCommercial-NoDerivatives 4.0 International License, which permits any non-commercial use, sharing, distribution and reproduction in any medium or format, as long as you give appropriate credit to the original author(s) and the source, provide a link to the Creative Commons licence, and indicate if you modified the licensed material. You do not have permission under this licence to share adapted material derived from this article or parts of it. The images or other third party material in this article are included in the article's Creative Commons licence, unless indicated otherwise in a credit line to the material. If material is not included in the article's Creative Commons licence and your intended use is not permitted by statutory regulation or exceeds the permitted use, you will need to obtain permission directly from the copyright holder. To view a copy of this licence, visit <http://creativecommons.org/licenses/by-nc-nd/4.0/>.

© The Author(s) 2025

¹School of Energy and Environment, City University of Hong Kong, Hong Kong, China. ²State Key Laboratory of Water Resources and Hydropower Engineering Science, Wuhan University, Wuhan, China. ³School of Fashion and Textiles, The Hong Kong Polytechnic University, Hong Kong, China. ⁴Department of Chemical Engineering, KU Leuven, Leuven, Belgium. ⁵Department of Chemistry, Tsinghua University, Beijing, China. ⁶Energy and Electricity Research Center, International Energy College, Jinan University, Guangdong, China. ⁷Chemical and Environmental Engineering, School of Engineering, RMIT University, Melbourne, Victoria, Australia. ⁸Yantai Research Institute, Harbin Engineering University, Yantai, Shandong, China. ⁹Guangdong Laboratory of Artificial Intelligence and Digital Economy (SZ), School of Biomedical Engineering, Shenzhen University, Shenzhen, PR China. ¹⁰Department of Engineering Science, University of Oxford, Oxford, United Kingdom. ¹¹Department of Chemical and Biological Engineering, The Hong Kong University of Science and Technology, Hong Kong, China. ¹²Department of Civil Engineering, The University of Hong Kong, Hong Kong, China. ¹³Kavli Institute for Nanoscience Discovery, Department of Physiology, Anatomy, & Genetics, University of Oxford, Oxford, United Kingdom. ✉ e-mail: ganglu2-c@my.cityu.edu.hk; alicia.kjan@ust.hk; shuang.zheng@dpag.ox.ac.uk